Thermohydraulic Modeling of Microchannel Cold Plates for Two-Phase Data Center Cooling

Qingyang Wang*, Trevor A. Whitaker, Akshith Narayanan, Serdar Ozguc, Jacob D. Moore, Richard W. Bonner III

Accelsius, Austin, TX, USA
*qwang@accelsius.com

***Abstract*— As artificial intelligence workloads continue to drive increasing power densities in processors and server racks, effective thermal management has become critical for data centers. High-performance cooling technologies are essential to sustain the advancement of next-generation processors and rack architectures. Among various approaches, pumped two-phase direct-to-chip cooling leverages the high heat transfer coefficient (HTC) associated with boiling, offering superior thermal performance together with intrinsic reliability and scalability. While future processors with higher heat fluxes may require two-phase cold plate designs incorporating capillary structures or surface enhancements, current processor heat flux levels remain relatively moderate. Consequently, skived-fin cold plates based on microchannel flow boiling are widely adopted due to their low-cost manufacturability, broad vendor availability, and sufficient thermal performance.**

Although microchannel flow boiling has been extensively studied at the channel and component levels, thermohydraulic characterization of two-phase cold plates under realistic operating conditions consistent with data center system-level boundary conditions remains comparatively limited. In this work, a correlation-based modeling framework is developed to investigate the thermohydraulic characteristics of skived-fin microchannel cold plates over a wide range of operating conditions. Rather than focusing on local or channel-wall HTCs, an effective footprint HTC is defined based on the average wall temperature and outlet fluid temperature, incorporating heat transfer, pressure drop, and inlet subcooling effects. This metric represents the global thermal performance of the cold plate, isolates system-level boundary conditions, and is more easily accessible in practical product development and characterization processes. Model inputs are selected to reflect parameters that are readily available under realistic operating conditions. The effective footprint HTC is evaluated as a function of footprint heat flux, apparent inlet subcooling, nominal exit quality, and channel geometric parameters, and the effects of different parameters are analyzed and discussed. This work provides practical insights into parametric optimization for microchannel cold plate design, contributing to the development of efficient two-phase cooling solutions for next-generation high-performance data centers.

Keywords*— *two-phase, flow boiling, microchannel, cold plate

I. INTRODUCTION

The rapid advancement of artificial intelligence (AI) has driven an unprecedented increase in compute density and power consumption in modern data centers, particularly due to the widespread deployment of high-performance GPUs and AI accelerators whose power levels and heat fluxes exceed the thermal limits of traditional air and single-phase liquid cooling solutions. Pumped two-phase (2P) direct-to-chip (DTC) cooling addresses this challenge by leveraging the latent heat of vaporization to efficiently remove large heat loads while maintaining near-isothermal device temperatures, which is critical for performance, reliability, and lifetime in AI workloads. In addition, the dielectric nature of the refrigerant coolant used in 2P DTC systems mitigates the risk of catastrophic electronic damage in the event of leakage. As AI systems continue to scale in both size and power, pumped 2P DTC cooling is emerging as a necessary technology to sustain performance growth while improving data center sustainability, energy efficiency, and equipment safety.

2P DTC data center cooling has seen great progress in the past several years. An OCP (Open Compute Project) white paper [1] provided an introduction of 2P DTC cooling and an overview of its ecosystem. A framework is established [2] to systematically break down and evaluate the different thermal contributions to 2P DTC cooling system performance. At the cold plate level, high power and high heat flux cooling have been demonstrated with different choices of refrigerant [3-5]. Further promising enhancement is demonstrated by optimizing the microchannel geometry [6], or by delivering fluid directly to the package and thereby removing the resistance from thermal interface materials (TIMs) [7, 8]. At the system level, 2P flow management has also been investigated and solutions to mitigate flow maldistribution have been discussed [9].

It has been demonstrated that for 2P heat transfer, advanced structures with delicate design can achieve superior heat transfer performance due to various enhancement mechanisms such as capillary assisted liquid delivery, guided and promoted vapor venting, and reduced liquid conduction characteristic length [10-12]. Nonetheless, microchannels formed by parallel straight fins with sub-mm feature size (fin thickness) and

spacing are most used for current 2P cold plates. This is majorly due to the readily available copper skiving process capable of producing microchannels with low cost and high throughput, as well as the sufficiently high performance offered by microchannel flow boiling. Even just using the existing single-phase (1P) microchannel cold plates for 2P cooling without any 2P specific modifications, the cold plate performs better in 2P mode than in 1P mode [13, 14]. In another word, one can use a universal cold plate for both 1P and 2P cooling, which helps the adoption of 2P DTC technology by reducing the time-to-market and total cost of ownership [13, 14]. Moreover, the use of microchannels yields the gravity effect negligible, thereby allowing the cold plates to operate under different orientations to meet the requirements for different server and rack architectures [15, 16].

Although microchannel flow boiling has been extensively studied at the channel and component levels over the past several decades [17-19], thermohydraulic characterization of 2P cold plates under realistic operating conditions consistent with data center system-level boundary conditions remains comparatively limited. Prior mechanistic models [20, 21] have largely emphasized detailed channel-scale transport modeling rather than footprint-level performance representation aligned with system boundary conditions. In this work, a correlation-based modeling framework is developed to investigate the thermohydraulic characteristics of 2P microchannel cold plates over a wide range of operating conditions. Rather than focusing on local or channel-wall heat transfer coefficients (HTCs), an effective footprint HTC is defined based on the average wall temperature and outlet fluid temperature, incorporating heat transfer, pressure drop, and inlet subcooling effects [22]. This metric represents the global thermal performance of the cold plate, isolates system-level boundary conditions, and is readily accessible in practical product development and characterization processes. Model inputs are selected to reflect parameters that are directly available under realistic operating conditions. The effective footprint HTC is evaluated as a function of footprint heat flux, apparent inlet subcooling, nominal exit quality, and channel geometric parameters, and the effects of different parameters are analyzed and discussed. This work provides practical insights into parametric optimization of microchannel cold plate design, contributing to the development of efficient two-phase cooling solutions for next-generation high-performance data centers.

II. Model

A. Model Framework

A thermofluidic model is developed to predict the heat transfer performance of a microchannel 2P cold plate made of copper. The model is based on a pass-through microchannel configuration, as shown in Figure 1. The cold plate is assumed to have a plurality of microchannels in parallel, which can be scalably manufactured through skiving. In this work, identical geometries and uniform thermal and fluid distributions between the parallel microchannels are assumed, and a single channel unit cell is analyzed (dashed blue box in Figure 1). Uniform heat flux across the footprint area is assumed as the boundary

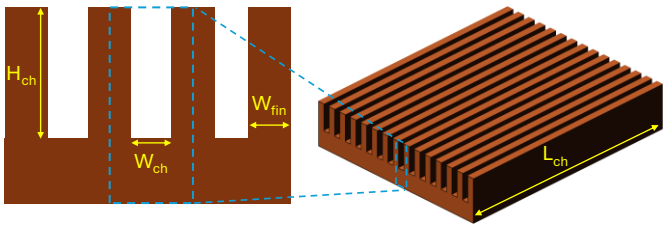

Fig. 1. Schematic of the modeled microchannel configuration.

condition. Although not shown in the schematic in Figure 1, the channels are all closed at the top by a flat roof, representing the case when a skived-fin base plate is brazed with a lid, where the tips of all the fins are bonded to the lid bottom surface. The important geometrical parameters are annotated in Figure 1, where W_{fin}, W_{ch}, H_{ch}, L_{ch} represent the width (thickness) of the fin, the width of the channel, the height of the channel, and the length of the channel, respectively. Although this model is based on a pass-through configuration, it should also be applicable to represent manifold-microchannel cold plate designs [16, 23], where the effective channel length between liquid and vapor manifolds is taken as L_{ch}. In all cases modeled in this work, $W_{fin} = W_{ch}$ is implemented, which represents a common skiving design with a 1:1 fin-spacing ratio.

Under practical operations of a cold plate in a pumped 2P DTC cooling system, the outlet temperature of the cold plate is dictated by the downstream pressure drop and the system operating conditions, and is independent of the cold plate itself [2, 22]. Hence, in the current model, the cold plate is given a prescribed outlet temperature T_{out} . The channel outlet temperature is assumed equal to T_{out}, which assumes minimal pressure drop from channel outlet to cold plate outlet. In this work, T_{out} is fixed at 45 °C, corresponding to a typical 2P DTC system working condition. The refrigerant is taken to be R515B, and its thermophysical properties are all evaluated at T_{out} and assumed temperature-independent given the small range of temperature variation along the channel. All properties are obtained from NIST REFPROP database [24].

Due to the downstream 2P pressure drop, there is an inevitable subcooling at the cold plate inlet [2], i.e., $T_{in} < T_{out}$. Given the small channel size and the small subcooling under practical operating conditions, subcooled boiling is neglected and uniform fluid temperature at each axial location of the channel is assumed. For cases involving large inlet subcooling or strong transverse temperature gradients, more detailed mechanistic treatment may be required and is beyond the scope of this work. Consequently, the fluid flow in the microchannel can be divided into two segments: a subcooled 1P segment where the fluid remains liquid, and a 2P segment for saturated flow boiling where the fluid is saturated and vaporized [22]. The fluid temperature along the channel would first increase in the 1P segment due to sensible heating, and then decrease in the 2P segment due to the drop of local saturation pressure, as shown in Figure 2 schematically. The fluid temperature at the boundary between 1P and 2P segments T_b is dependent on the channel geometric parameters and cold plate working conditions (such as flow rate, exit quality, heat flux, etc.).

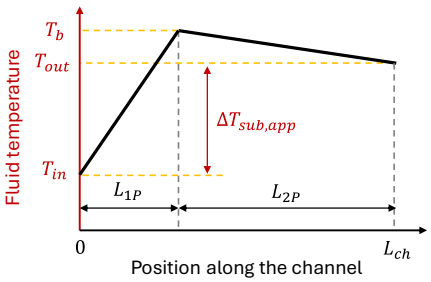

Fig. 2. Fluid temperature variation along the channel.

Consequently, under the assumption of constant footprint heat flux, the 2P segment length would also be different even with fixed T_{out}, T_{in}, and L_{ch}. However, during cold plate development and testing, the most accessible fluid temperatures are T_{in} and T_{out}, whose measurements are not intrusive to the heat transfer inside the cold plate. Therefore, although the saturation temperature variation along the channel can be captured in this model, an apparent subcooling $\Delta T_{sub,app}$ is given as the model input, defined by $T_{out} - T_{in}$ as shown in Figure 2, since it depends only on system conditions, has been commonly used, and is easily obtainable practically.

B. Model Formulation

The input parameters for the model include channel geometric parameters shown in Figure 1, the channel outlet temperature T_{out}, the apparent inlet subcooling $\Delta T_{sub,app}$, the footprint heat flux q''_{fp}, and the nominal vapor quality x_{nom}. The output of the model yields an effective footprint HTC value calculated using the average wall temperature, outlet fluid temperature, and footprint heat flux. All input parameters are common design parameters used for 2P systems, which require no specific knowledge of the actual heat transfer characteristics before the design. Besides the channel geometries, all other input parameters are either determined by system characteristics or used for system design, and they are independent of the specific cold plate used. The output effective footprint HTC is also easily measurable in cold plate testing without intrusive measurements, providing a quick and easy way to stack up the thermal resistances in a 2P cold plate [22].

The nominal exit vapor quality is a parameter commonly used in system level design to determine coolant flow rate, defined by

$$x_{nom} = \frac{Q}{\dot{m} h_{fg}} \tag{1}$$

where Q is the total thermal power, $\dot{m}$ is the fluid mass flow rate, and h_{fg} is the refrigerant latent heat. The nominal exit quality assumes no inlet subcooling and the thermal power is completely dissipated through phase change.

Given the nominal exit quality, the mass flow rate through a single channel in the analyzed unit cell can be calculated by

$$\dot{m}_{ch} = \frac{Q_{cell}}{x_{nom} h_{fg}} \tag{2}$$

in which the total heat per unit cell is obtained as

$$Q_{cell} = q''_{fp}(W_{fin} + W_{ch})L_{ch} \tag{3}$$

The HTCs along the two segments are modeled separately as detailed later. With uniform footprint heat flux, the lengths of the 1P and 2P segments are

$$L_{1P} = L_{ch}\phi_{1P} \tag{4}$$

$$L_{2P} = L_{ch}\phi_{2P} \tag{5}$$

where the fractions of 1P and 2P cooling are

$$\phi_{1P} = \frac{\dot{m}_{ch} c_p (T_b - T_{in})}{Q_{cell}} \tag{6}$$

$$\phi_{2P} = 1 - \phi_{1P} \tag{7}$$

C. Boundary of 1P/2P

As mentioned before, T_b is dependent on the parameters and working conditions. An iterative calculation is performed to determine the boundary separating the 1P and 2P segments. An initial guess for T_b is given, and L_{2P} is then meshed into elements. The local pressure at the boundary point is obtained by accumulating the 2P pressure drop of each mesh element and marching backwards from the known outlet condition.

For each mesh element represented by subscript j, the frictional pressure drop of the 2P flow is calculated based on homogeneous flow assumption [25]. The average quality $x_{ave,j}$ between the entrance and the exit of each mesh element is used to obtain 2P mixture density and viscosity as

$$\rho_{m,j} = \left(\frac{x_{ave,j}}{\rho_v} + \frac{1 - x_{ave,j}}{\rho_l}\right)^{-1} \tag{8}$$

$$\mu_{m,j} = \left(\frac{x_{ave,j}}{\mu_v} + \frac{1 - x_{ave,j}}{\mu_l}\right)^{-1} \tag{9}$$

in which ρ and μ represent fluid density and viscosity, respectively, and subscripts v and l represent vapor and liquid phases, respectively. The Reynolds number is calculated by

$$Re_{m,j} = \frac{G_{ch} d_h}{\mu_{m,j}} \tag{10}$$

where the G_{ch} is the channel mass flux and d_h is the channel hydraulic diameter,

$$G_{ch} = \frac{\dot{m}_{ch}}{W_{ch} H_{ch}} \tag{11}$$

$$d_h = \frac{2 W_{ch} H_{ch}}{W_{ch} + H_{ch}} \tag{12}$$

The frictional pressure drop along the mesh element length $L_{2P,j}$ is calculated using the Darcy-Weisbach equation,

$$\Delta P_{fr,j} = \frac{L_{2P,j} f_{m,j} G_{ch}^2}{2 d_h \rho_{m,j}} \tag{13}$$

in which the friction factor is obtained as

$$f_{m,j} = \begin{cases} 4Po/Re_{m,j}, & \text{if } Re_m \le 2300 \\ \left(0.790 \ln Re_{m,j} - 1.64\right)^{-2}, & \text{if } Re_m > 2300 \end{cases} \tag{14}$$

For fully developed laminar flow in a rectangular channel with cross-sectional aspect ratio of α_c (ratio of short side to long side), the Poiseuille number is obtained from a polynomial fitting equation [26],

$$Po = 24(1 - 1.3553\alpha_c + 1.9467{\alpha_c}^2 - 1.7012{\alpha_c}^3 + 0.9564{\alpha_c}^4 - 0.2537{\alpha_c}^5) \tag{15}$$

The total frictional pressure drop along the 2P segment $\Delta P_{2P,fr}$ is obtained by summing the $\Delta P_{fr,j}$ of each mesh element,

$$\Delta P_{2P,fr} = \sum \Delta P_{fr,j} \tag{16}$$

The acceleration pressure drop along the 2P segment is calculated as

$$\Delta P_{2P,ac} = G_{ch}^2 \left(\frac{1}{\rho_{out}} - \frac{1}{\rho_l}\right) \tag{17}$$

in which the outlet 2P mixture density is calculated by

$$\rho_{out} = \left(\frac{x_{out}}{\rho_v} + \frac{1 - x_{out}}{\rho_l}\right)^{-1} \tag{18}$$

and the outlet quality is obtained as

$$x_{out} = \frac{Q_{cell}\phi_{2P}}{\dot{m}_{ch} h_{fg}} \tag{19}$$

The fluid pressure at the boundary between 1P and 2P segments is obtained by adding the total pressure drop along the 2P segment to the outlet saturation pressure,

$$P_b = P_{out} + \Delta P_{2P,fr} + \Delta P_{2P,ac} \tag{20}$$

and a new T_b value is then obtained from the saturation curve of the fluid at P_b. The newly obtained T_b is compared with the initial guessed T_b and iterative calculation is performed until the T_b value converges.

D. Channel HTCs

For both the 1P and 2P segments, an average channel HTC is obtained based on classical correlations. For 2P HTC, since the correlations were developed from experimental data that inherently reflect liquid-vapor interactions including flow regime transitions and phase slip effects, the present model captures the global thermohydraulic performance trends of microchannel flow boiling without explicitly resolving detailed flow-structure behavior.

Due to the small channel size investigated here, the 1P segment flow remains laminar. The HTC of the 1P segment is obtained using correlations for thermally developing laminar flow considering the entrance effect. The local Nusselt number is obtained as a function of the channel aspect ratio α_c and the dimensionless location z^* from the entrance [26],

$$Nu_z = f(\alpha_c, z^*) \tag{21}$$

$$z^* = \frac{z}{Re_l Pr_l d_h} \tag{22}$$

$$Re_l = \frac{G_{ch} d_h}{\mu_l} \tag{23}$$

in which z is the distance from the entrance, Re_l is the Reynolds number of 1P segment, and Pr_l is the liquid Prandtl number. The function in Eq. (21) is obtained from Ref. [26] for specific tabulated α_c values, and interpolated for general α_c values unavailable in the table. The 1P segment is also meshed, the local Nu_z is calculated for each mesh element, and then the 1P segment Nu_{1P} is taken as the average of Nu_z along the 1P length. The HTC of 1P segment is subsequently obtained as

$$h_{1P} = \frac{Nu_{1P} k_l}{d_h} \tag{24}$$

where k_l is the liquid thermal conductivity.

The 2P segment heat transfer is calculated using the Kim and Mudawar correlation [27]. For each mesh element j of the discretized 2P segment, the channel HTC is obtained as a superposition of nucleate boiling and convective boiling HTCs as

$$h_{2P,j} = \sqrt{{h_{nb,j}}^2 + {h_{cb,j}}^2} \tag{25}$$

The overall 2P HTC h_{2P} is taken as the average of the $h_{2P,j}$ for all mesh elements along the 2P length. The subscript j is omitted in the following equations for simplicity. The nucleate boiling dominant HTC is obtained as

$$h_{nb} = \left[2345 \left(Bo \frac{P_H}{P_F}\right)^{0.70} P_R^{0.38} (1 - x_{ave})^{-0.51}\right] \times \left(0.023 Re_f^{0.8} Pr_l^{0.4} \frac{k_l}{d_h}\right) \tag{26}$$

in which Bo is the boiling number,

$$Bo = \frac{q_H''}{G_{ch} h_{fg}} \tag{27}$$

where q_H'' is the effective heat flux average over heated perimeter of the channel, and fin efficiency is taken into consideration:

$$q_H'' = q_{fp}'' \frac{W_{ch} + W_{fin}}{W_{ch} + 2\eta H_{ch}} \tag{28}$$

The fin efficiency η is calculated as

$$\eta = \frac{\tanh(mH_{ch})}{mH_{ch}} \tag{29}$$

$$m = \sqrt{\frac{2h_{2P}}{k_{Cu} W_{fin}}} \tag{30}$$

where k_{Cu} is the copper thermal conductivity. An average fin efficiency for the 2P segment is used. An iterative solution is performed to converge the fin efficiency value since it dependes on the unknown h_{2P}. P_H and P_F are the heated perimeter and wetted perimeter of the channel cross section, respectively:

$$P_H = W_{ch} + 2\eta H_{ch} \tag{31}$$

$$P_F = 2(W_{ch} + H_{ch}) \tag{32}$$

$P_R = P/P_{cr}$ is the reduced pressure where P_{cr} is the fluid critical pressure. Given the small variation of fluid pressure relative to the critical pressure, the fluid pressure P is taken as the outlet saturation pressure P_{out} for all cases to obtain P_R. The superficial liquid Reynolds number Re_f in the Dittus-Boelter relation is calculated by

$$Re_f = \frac{G_{ch}(1 - x_{ave}) d_h}{\mu_l} \tag{33}$$

The convective boiling dominant HTC is obtained as

$$h_{cb} = \left[5.2 \left(Bo \frac{P_H}{P_F}\right)^{0.08} We_{fo}^{-0.54} + 3.5 \left(\frac{1}{X_{tt}}\right)^{0.94} \left(\frac{\rho_v}{\rho_l}\right)^{0.25}\right] \times \left(0.023 Re_f^{0.8} Pr_l^{0.4} \frac{k_l}{d_h}\right) \tag{34}$$

where the Weber number We_{fo} is calculated as

$$We_{fo} = \frac{G_{ch}^2 d_h}{\rho_l \sigma} \tag{35}$$

in which σ is the fluid surface tension. The Lockhart–Martinelli parameter X_{tt} is obtained as

$$X_{tt} = \left(\frac{\mu_l}{\mu_v}\right)^{0.1} \left(\frac{1 - x_{ave}}{x_{ave}}\right)^{0.9} \left(\frac{\rho_v}{\rho_l}\right)^{0.5} \tag{36}$$

The above Kim-Mudawar correlation [27] is applicable for pre-dryout regimes in saturated flow boiling. With high heat flux, large channel length, and large vapor quality, dryout incipience or partial dryout may occur [28], which yields lowered HTC. The dryout incipience quality is obtained as [28]

$$x_{di} = 1.4We_{fo}^{0.03} P_R^{0.08} - 15.0 \left(Bo \frac{P_H}{P_F}\right)^{0.15} Ca^{0.35} \left(\frac{\rho_v}{\rho_l}\right)^{0.06} \tag{37}$$

where the capillary number is calculated by

$$Ca = \frac{\mu_l G_{ch}}{\rho_l \sigma} \tag{38}$$

After dryout incipience, the local HTC decreases appreciably but still provides sufficient cooling capacity until dryout completion where the liquid film is completely evaporated. Predicting post-dryout-incipience HTC is difficult as it depends on local flow pattern and adjacent heat spreading. In this work, if $x_{out} > x_{di}$ indicating dryout incipience happens within the channel, we assume that the local HTC experiences an exponential decay as a function of quality starting from dryout incipience, which is a pragmatic reduced-order representation of the progressive degradation in heat transfer. Consequently, for any mesh element with a quality $x_{ave,j}$ larger than x_{di},

$$h_{2P,j} = h_{di} e^{-C_d (x_{ave,j} - x_{di})} \tag{39}$$

where h_{di} is the 2P HTC calculated by Eq. (25) for the mesh element j corresponding to a quality right before exceeding x_{di} (i.e., $x_{ave,j} \leq x_{di}$ and $x_{ave,j+1} > x_{di}$). The constant C_d in Eq. (39) is obtained by prescribing another combination of quality-HTC data point. We assume the following lower bound HTC h_{lb} at a quality of 1,

$$h_{lb} = 0.023 Re_v^{0.8} Pr_v^{0.4} \frac{k_v}{d_h} \tag{40}$$

where

$$Re_v = \frac{G_{ch} d_h}{\mu_v} \tag{41}$$

k_v, Pr_v, and μ_v are the thermal conductivity, Prandtl number, and viscosity of vapor phase, respectively. The lower bound HTC represents pure vapor convection inside the channel, corresponding to complete dryout. Therefore, the constant C_d in Eq. (39) is represented by

$$C_d = \frac{\ln(h_{di}/h_{lb})}{1 - x_{di}} \tag{42}$$

E. Effective Footprint HTC

For practical applications, a footprint HTC yields an area-specific thermal resistance for surface-to-fluid heat transfer, and allows easy estimation of the overall cold plate performance by assuming one-dimensional heat transfer and in-series thermal resistance network (including thermal resistances from TIM, base conduction, and boiling) [22]. An effective footprint HTC calculated using the cold plate outlet temperature as the characteristic fluid temperature is of most practical convenience. In this work, after the channel HTCs for 1P and 2P segments are separately obtained, the wall temperature of the 1P and 2P segments are calculated individually using the average fluid temperature within each segment (see Figure 2):

$$T_{w,1P} = \frac{q''_{fp}}{h_{1P}} \frac{W_{ch} + W_{fin}}{W_{ch} + 2\eta_{1P} H_{ch}} + \frac{T_{in} + T_b}{2} \tag{43}$$

$$T_{w,2P} = \frac{q''_{fp}}{h_{2P}} \frac{W_{ch} + W_{fin}}{W_{ch} + 2\eta_{2P} H_{ch}} + \frac{T_b + T_{out}}{2} \tag{44}$$

where η_{1P} and η_{2P} are the fin efficiencies of the 1P and 2P segments, respectively. The overall average wall temperature is obtained as their weighted average,

$$T_{w,ave} = \phi_{1P} T_{w,1P} + \phi_{2P} T_{w,2P} \tag{45}$$

The effective footprint HTC is finally obtained using the average wall temperature, the outlet fluid temperature, and the footprint heat flux,

$$h_{fp,eff} = \frac{q''_{fp}}{T_{w,ave} - T_{out}} \tag{46}$$

In addition to dryout, premature critical heat flux (CHF) associated with flow instabilities and two-phase critical flow (choking) are two other limits of flow boiling and should be prevented [29]. The Qu and Mudawar model [30] is used to calculate the premature CHF value as

$$q''_{CHF} = 33.43 G_{ch} h_{fg} \left(\frac{\rho_v}{\rho_l}\right)^{1.11} We_L^{-0.21} \left(\frac{L_{ch}}{d_h}\right)^{-0.36} \tag{47}$$

where the channel-length-based Weber number is

$$We_L = \frac{G_{ch}^2 L_{ch}}{\rho_l \sigma} \tag{48}$$

For choked flow, following Kim and Mudawar [31], the Homogeneous Frozen Model [32] without flashing gives the critical mass flux as

$$G_{crit} = \left\{ -\left[x_{out} \frac{dv_v}{dP} + (1 - x_{out}) \frac{dv_l}{dP} \right] \right\}^{-0.5} \tag{49}$$

in which the outlet quality is used since it corresponds to the condition most prone to choking. $v = 1/\rho$ is the volume of respective phases. The derivative terms for both phases are obtained as

$$\frac{dv}{dP} = -\kappa_T v \tag{50}$$

in which κ_T is the isothermal compressibility of respective phases. The calculated premature CHF heat flux is compared with the 2P effective wall heat flux q''_H, and the calculated critical mass flux is compared with the channel mass flux G_{ch}. When $q''_H > q''_{CHF}$ or $G_{ch} > G_{crit}$, the effective footprint HTC is set to zero to exclude premature CHF and choking conditions.

F. Model Validation

The developed model is validated by comparing its prediction with the experimentally measured data. Figure 3 shows a validation plot for 63 experimental data points obtained from a microchannel cold plate used in Ref. [5], tested using R515B with different operating conditions, where heat flux varies in the range of 10~180 W/cm^2. Most data points fall

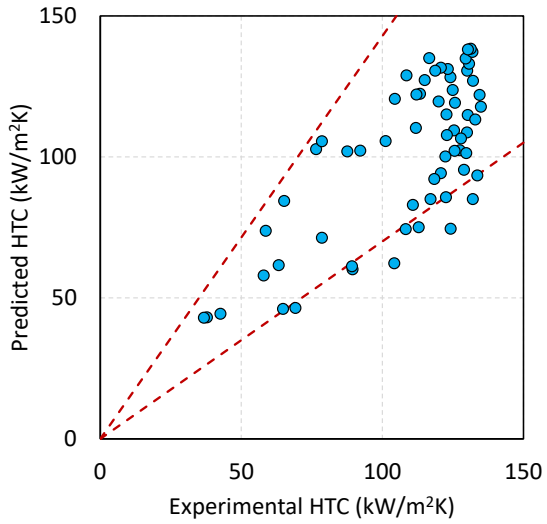

Fig. 3. Comparison between model predicted and experimentally measured effective footprint HTCs. The red dashed lines represent ±30% deviation.

within the ±30% deviation bounds indicated by the red dashed lines. The mean relative error e_R, mean absolute relative error e_A, and root-mean-square relative error e_S are used to quantify the validation, which are defined as

$$e_R = \frac{1}{n}\sum_{i=1}^{n} e_i \tag{51}$$

$$e_A = \frac{1}{n}\sum_{i=1}^{n} |e_i| \tag{52}$$

$$e_S = \sqrt{\frac{1}{n}\sum_{i=1}^{n} e_i^2} \tag{53}$$

where e_i is the relative error for each data point,

$$e_i = \frac{h_{fp,pre} - h_{fp,exp}}{h_{fp,exp}} \tag{54}$$

in which $h_{fp,pre}$ and $h_{fp,exp}$ are the predicted and experimental measured effective footprint HTCs, respectively. For the 63 data points, the model yields e_R = -6.1%, e_A = 16.2%, and e_S = 19.8%, indicating good agreement with the experimental data. More comprehensive validation across a broader range of channel geometries will be conducted in future work.

III. Results and Discussion

In the following parametric sweeps, one specific input parameter combination is used to establish a comparison baseline. Unless otherwise specified, the input parameters of the baseline case are: footprint heat flux q''_{fp} =100 W/cm^2, nominal exit quality x_{nom}=0.7, apparent inlet subcooling $\Delta T_{sub,app}$=3 °C, channel width W_{ch} =0.2 mm, channel height H_{ch} =2 mm, and channel length L_{ch} =30 mm. The baseline input parameters represent a typical cold plate working condition. The variations with and the effects of different input parameters are analyzed

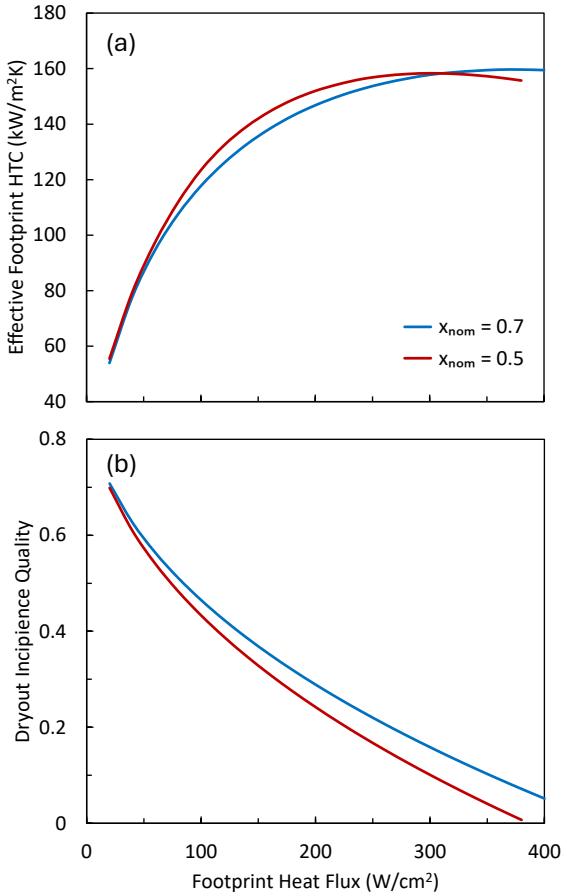

Fig. 4. (a) Effective footprint HTC and (b) dryout incipience quality as a function of footprint heat flux, under two different nominal exit quality conditions, with apparent inlet subcooling $\Delta T_{sub,app}$=3 °C, channel width W_{ch} =0.2 mm, channel height H_{ch} =2 mm, and channel length L_{ch} =30 mm.

and discussed below. Although channel hydraulic diameter can provide a collective representation of the channel size, the channel width and channel height are analyzed separately below since they serve as the parameters directly used in practical design and manufacturing.

A. *Footprint Heat Flux*

Figure 4(a) shows the effective footprint HTC as a function of footprint heat flux. The blue curve represents the conditions where except the sweeping footprint heat flux, all other parameters equal to the baseline case. The red curve represents the conditions where the nominal exit quality is changed to 0.5 while all other parameters are kept the same as the baseline. It shows that effective footprint HTC first increases and then decreases with footprint heat flux, resulting in a peak effective footprint HTC. The initial increase of effective footprint HTC with footprint heat flux can be attributed to the increasing channel HTC. At lower heat flux levels, nucleate boiling is enhanced with increasing heat flux, which yields higher 2P segment HTC. Given a fixed channel geometry, higher footprint heat flux also results in higher mass flux in the channel, which enhances both the 1P and 2P channel HTC due

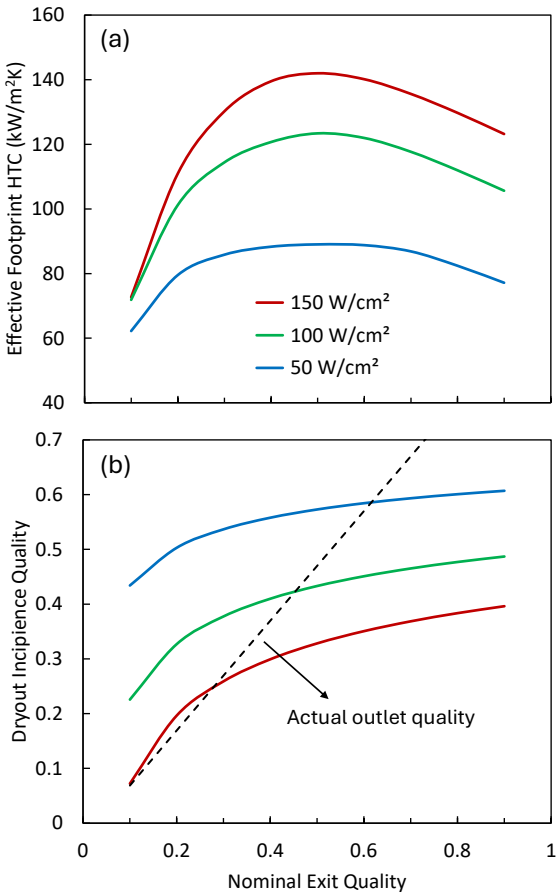

Fig. 5. (a) Effective footprint HTC and (b) dryout incipience quality as a function of nominal exit quality, under three different footprint heat flux conditions, with apparent inlet subcooling $\Delta T_{sub,app}$=3 °C, channel width W_{ch} =0.2 mm, channel height H_{ch} =2 mm, and channel length L_{ch} =30 mm.

to enhanced convection. On the contrary, under high heat flux conditions, both the increase of heat flux and its resultant increase in the mass flux will yield a smaller dryout incipience quality, as shown in Figure 4(b). Consequently, with higher footprint heat flux, more flow length will have inefficient post-dryout-incipience heat transfer, resulting in reduced effective footprint HTC. Additionally, the increased heat flux (and hence mass flux) causes higher 2P pressure drop along the channel, which yields a higher average boiling temperature given the same outlet temperature (see Figure 2). This translates to a higher wall temperature even for the same channel HTC, contributing to a reduced effective footprint HTC. The trade-off among these effects results in the non-monotonic trend in Figure 4(a).

The two curves corresponding to different nominal qualities of 0.7 and 0.5 cross over in Figure 4(a). At medium heat fluxes, the lower nominal quality of 0.5 yields a higher effective footprint HTC, due to enhanced convection resulting from higher mass flux. Conversely, at high heat fluxes, the lower nominal quality condition yields a lower effective footprint HTC, due to the lower dryout incipience quality as shown in Figure 4(b) causing reduced 2P channel HTC. Detailed discussion about the variation of effective footprint HTC with nominal quality will be discussed in the following section.

B. Nominal Quality

Figure 5(a) shows the variation of effective footprint HTC with varying nominal quality ranging from 0.1 to 0.9. Three different footprint heat flux conditions are modeled (50, 100, 150 W/cm^2), and other input parameters are kept fixed as the baseline case. Comparing the three curves in Figure 5(a), for a given nominal quality, the effective footprint HTC increases with heat flux in the range of the three heat fluxes modeled, which is also shown in Figure 4(a) and the reasons are discussed before.

For a given heat flux, the effective footprint HTC first increases and then decreases with nominal quality. The peak effective footprint HTC is achieved when the nominal quality is in the range of 0.4~0.6, which varies slightly with different conditions. This agrees with our experimental results [5] and can be attributed to the trade-off between different effects. At low nominal quality conditions, decreasing the nominal quality increases the excessive fluid flow rate, which results in a larger fraction of inefficient 1P convective cooling and hence a lower effective footprint HTC. At high nominal quality above 0.6, increasing nominal quality causes the heat transfer to be more prone to dryout. As shown in Figure 5(b), the nominal quality (and thus actual outlet quality shown by the black dashed line, which is slightly below nominal quality due to inlet subcooling) exceeds the dryout incipience quality towards the right side of the plot. Consequently, higher nominal quality results in more channel length working under post-dryout-incipience conditions with depreciated boiling HTC, causing a lower effective footprint HTC.

C. Apparent Subcooling

Figure 6(a) shows the variation of effective footprint HTC with apparent subcooling for four different cases, each with a different footprint heat flux and nominal quality combination. There is a clear monotonic decrease of effective footprint HTC with increasing apparent subcooling, which is intuitive since higher subcooling results in a larger fraction of 1P liquid convective cooling with worse heat transfer than saturated flow boiling. Figure 6(b) shows the 1P fraction as a function of apparent subcooling, where a general linear increasing trend is observed for each curve, as expected. One unintuitive observation is that when the apparent subcooling is zero, the 1P fraction is not zero. This is due to the fluid temperature variation inside the channel as shown in Figure 2. Even when the apparent subcooling is zero and the inlet and outlet temperatures are equal, the inlet is still subcooled due to higher local pressure P_b resulted from 2P segment pressure drop.

In Figure 6(a), for all curves, the effective footprint HTC decreases almost linearly with apparent subcooling at low apparent subcooling values. This is because under these conditions, heat dissipation is predominantly taken by the 2P segment, with a small 1P fraction below ~15% as shown in Figure 6(b). Under these conditions, the effective footprint HTC is approximately a linear superposition of 1P and 2P heat

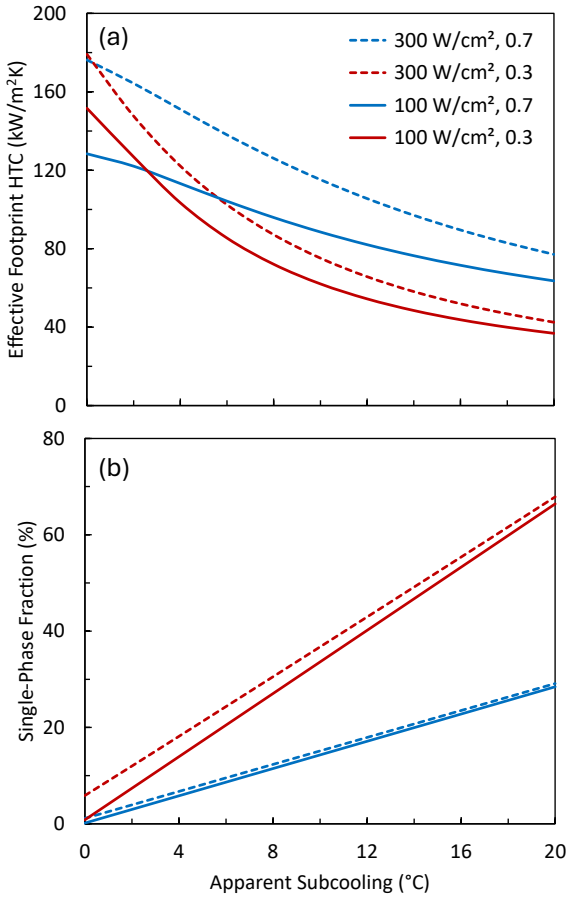

Fig. 6. (a) Effective footprint HTC and (b) 1P fraction as a function of apparent subcooling, under different footprint heat flux/nominal exit quality combinations, with channel width W_{ch} =0.2 mm, channel height H_{ch} =2 mm, and channel length L_{ch} =30 mm.

transfer weighted by their heat transfer length. The 1P fraction (and hence 1P segment length) is almost linearly dictated by apparent subcooling as shown in Figure 6(b). It can be further validated by the observation that given a nominal quality of 0.7, the higher heat flux of 300 W/cm^2 (dashed blue) has a steeper decreasing slope than the 100 W/cm^2 (solid blue) condition. This is due to the higher 2P channel HTC for high heat flux conditions and thus larger difference between 2P and 1P segment HTCs.

When the apparent subcooling increases or the nominal quality decreases (inducing higher mass flux), the linear decreasing trend of effective footprint HTC slows down and flattens, as shown in Figure 6(a). This can be attributed to the increasing dominance of 1P convection, since the 1P fraction exceeds ~20% under these conditions. Given the small channel size investigated in this work, the 1P convective heat transfer will be laminar in the channel and the entrance effect becomes small. Therefore, the 1P channel HTC can be represented by a constant value corresponding to fully developed laminar convection, which is independent of the flow rate and temperature conditions. However, despite the unchanged 1P channel HTC, the increasing subcooling provides a lower bulk fluid temperature for the 1P segment, rendering lower wall

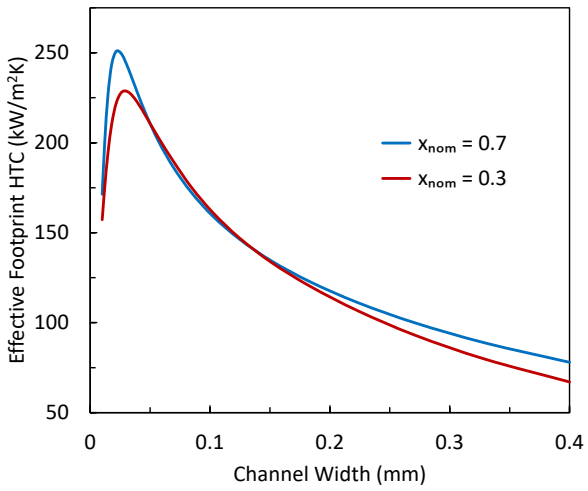

Fig. 7. Effective footprint HTC as a function of channel width, under two different nominal exit quality conditions, with footprint heat flux q''_{fp} = 100 W/cm^2, apparent inlet subcooling $\Delta T_{sub,app}$ =3 °C, channel height H_{ch} =2 mm, and channel length L_{ch} =30 mm.

temperature. If the apparent subcooling keeps increasing, the channel can be dominated or even fully occupied by 1P cooling, and the low bulk fluid temperature in the 1P segment can significantly reduce the average wall temperature, so that the effective footprint HTC flattens or even increases. In extreme cases, the 1P segment wall temperature can be smaller than the channel outlet temperature. With 1P dominance, this can lead to an average wall temperature smaller than outlet temperature, leading to a meaningless negative value for the effective footprint HTC. Such increase of and/or negative value of the effective footprint HTC is resulted from its mathematical definition, and does not indicate heat transfer enhancement or anomalous thermal behavior. Therefore, the current model is only applicable under low apparent subcooling conditions that are realistic, for example, when the 1P fraction is below an arbitrary ~20%.

D. Channel Width

Figure 7 shows the variation of effective footprint HTC with channel width, with two curves representing different nominal quality conditions of 0.3 and 0.7. The two curves display very similar values due to their more-or-less equal "distance" from the nominal quality of ~0.5 which corresponds to the peak effective footprint HTC (Figure 5(a)). Interestingly, with all other input parameters fixed, the effective footprint HTC shows a non-monotonic trend with channel width, with a peak performance achieved at sub-50 μm channel size.

It is straightforward that a reduced channel size corresponds to a higher in-channel HTC for 1P convection. For 2P microchannel flow boiling, the concept is still valid when the channel size is sufficiently large, where the flow boiling HTC increases almost the same way as 1P HTC with decreasing channel size. This is also shown by the Dittus-Boelter relation in Eqs. (26) and (34). However, when the channel width is too small, although the channel wall HTC may still see continuous increase over decreased channel size, the pressure drop increases

dramatically, which induces a significant saturation temperature drop along the flow, effectively raising the wall temperature. Therefore, from a cold plate application perspective, local HTC provides limited performance indication, since a high local channel HTC does not indicate a lower wall temperature in practical application. The effective footprint HTC defined using the outlet fluid temperature incorporates the pressure drop induced thermal resistance and can assess the thermohydraulic performance in a more comprehensive manner [22].

One effect not considered by the model is that when the channel size is sufficiently small, intermolecular forces can play an important role, suppressing or even preventing nucleation and vaporization. However, molecular effect is only expected to become significant for channel dimensions smaller than 0.01 mm [33] and is beyond the parameters investigated in this work. Therefore, for the range of channel width values readily achievable from skiving (>0.05 mm), the effect of channel HTC enhancement dominates over the effect of channel pressure drop increment, so that the effective footprint HTC monotonically increases with decreasing channel size, which is consistent with our previous experimental results [6].

E. Channel Height

Figure 8(a) shows the variation of effective footprint HTC with channel height given four different footprint heat flux/channel width combinations. For each given combination, the effective footprint HTC first increases and later decreases with increasing channel height, again indicating a trade-off between enhancement and deterioration effects. Figure 8(b) shows the fin efficiency of the 2P segment (η_{2P}) as a function of the channel height. The 2P fin efficiency is over ~70% with small channel height below 1 mm. Therefore, when the channel height is small, increasing the channel height provides additional heat transfer area, thereby increasing the effective footprint HTC. However, as the channel height increases beyond 2.5 mm, the fin efficiency drops down to below 50%, so that the increased physical area provided by increasing channel height contributes insignificantly to heat transfer due to depleted fin efficiency. On the contrary, increasing the channel height, given fixed footprint heat flux and channel width, reduces the channel mass flux, and consequently decreases the channel HTC for both 1P and 2P segments. Hence, when the channel height is large, as the channel height increases, the marginal enhancement of effective heat transfer area is overcome by the decrease of channel HTC, thereby showing a decreasing effective footprint HTC as a function of channel height. It is noted that the boundary between "small" and "large" is dependent on the working conditions and the channel geometries, as shown in Figure 8(a) where the peak effective footprint HTC is achieved at different channel height for different curves. The channel height corresponding to the peak effective footprint HTC is larger for larger channel width, as expected from fin efficiency analysis.

Another interesting observation in Figure 8(a) is that at small channel height conditions, given the same channel width, higher heat flux results in lower effective footprint HTC, where the dashed lines stay below the solid lines for either blue or red

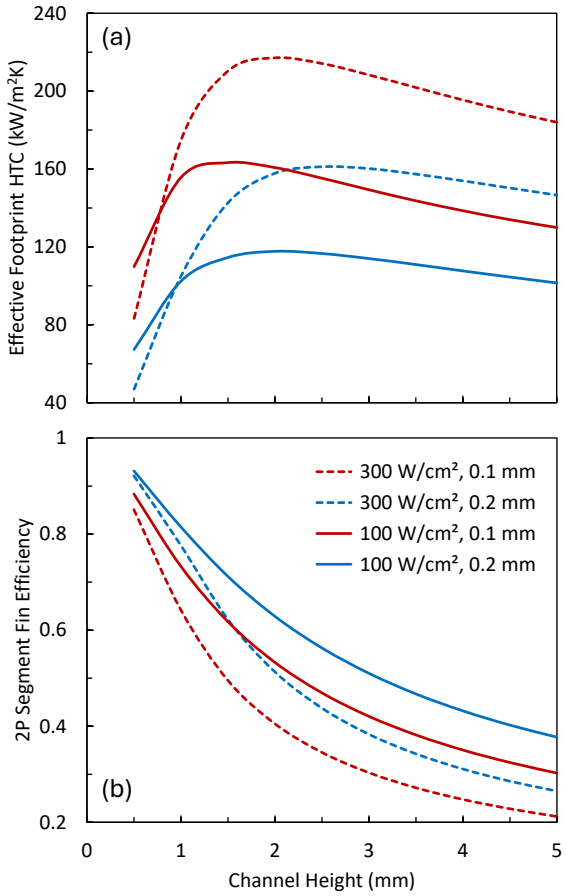

Fig. 8. (a) Effective footprint HTC and (b) 2P segment fin efficiency as a function of channel height, under different footprint heat flux/channel width combinations, with nominal exit quality x_{nom}=0.7, apparent inlet subcooling $\Delta T_{sub,app}$=3 °C, and channel length L_{ch} =30 mm.

colors on the very left of the plot. The reason can be attributed to the in-channel 2P pressure drop: with small channel height and high heat flux, the 2P segment pressure drop becomes significant and causes T_b to be much larger than T_{out}. Consequently, under small channel height conditions, higher heat flux results in a higher fluid temperature and consequently higher wall temperature. The same effect can be seen more clearly in Section F below. This can also explain the trend that the effective footprint HTC for higher heat flux conditions starts to drop at a larger channel height, i.e., the peak in Figure 8(a) appears at a larger channel height for dashed curves than solid curves. The reason is that for high heat flux conditions, the increase of channel height provides more channel cross-section area and alleviates the channel pressure drop, therefore delaying the start of effective footprint HTC deterioration.

F. Channel Length

Figure 9(a) shows the effective footprint HTC as a function of channel length for four combinations of footprint heat flux/channel width conditions. The effective footprint HTC shows an initial increasing trend and a later decreasing trend over channel length for each given combination. Given all other conditions fixed, increasing the channel length provides higher

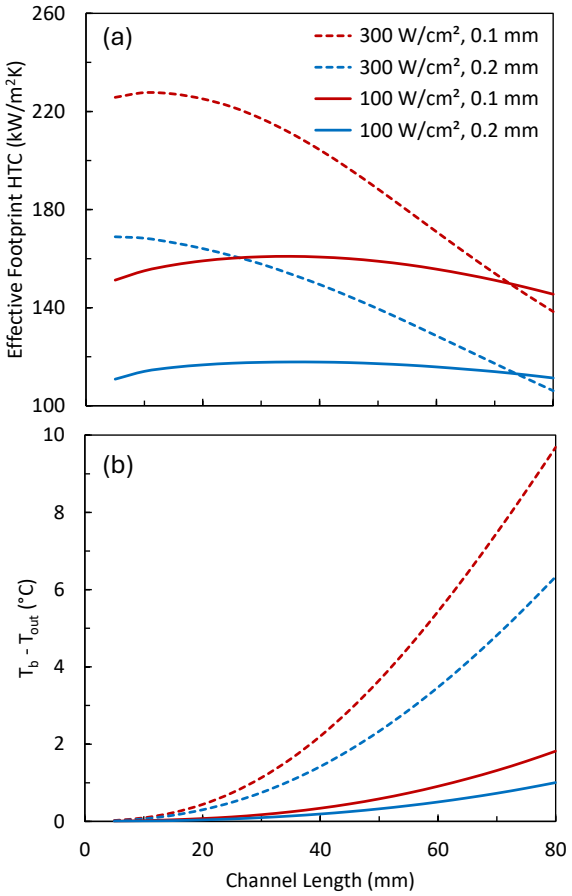

Fig. 9. (a) Effective footprint HTC and (b) 2P segment saturation temperature drop as a function of channel length, under different footprint heat flux/channel width combinations, with nominal exit quality x_{nom}=0.7, apparent inlet subcooling $\Delta T_{sub,app}$=3 °C, and channel height H_{ch} =2 mm.

channel mass flux which enhances in-channel convection for both 1P and 2P segments. Meanwhile, increasing the channel length also yields larger channel pressure drop, which raises the fluid temperature and effectively adds a pressure-drop-induced thermal resistance. The trade-off between these two effects results in the trend of the curves shown in Figure 9(a). It is also shown that for larger heat flux conditions, the effective footprint HTC starts to decrease at a smaller channel length. This is again attributed to the larger 2P pressure drop at higher heat flux conditions. Figure 9(b) shows the variation of the saturation temperature drop along the 2P segment ($T_b - T_{out}$, see Figure 2) with respect to channel length. With the largest channel length of 80 mm, pressure drop of the 2P segment results in an almost 10 °C rise of fluid temperature under the high heat flux/narrow channel condition, significantly raising the local wall temperature and reducing the effective footprint HTC.

IV. Summary

2P DTC cooling demonstrates superior thermal performance and enables effective cooling of high-heat-flux processors for next-generation AI data centers. Despite the performance advantages offered by more advanced structures, skived-fin microchannel cold plates remain widely employed due to their low-cost, high-throughput manufacturability. In this work, a thermohydraulic model is developed for microchannel-based 2P cold plates based on well established correlations. Using a single channel as the fundamental modeling unit, the channel length is divided into 1P and 2P regions, representing typical data center operating conditions for 2P cold plates with a finite inlet subcooling.

For improved practical applicability, the model input parameters are selected to correspond directly to cold plate design variables and system-level operating conditions, including footprint heat flux, nominal exit quality, apparent inlet subcooling, and channel geometric parameters such as width, height, and length. The model predicts an effective footprint HTC, calculated using the outlet fluid temperature, which accounts for the combined effects of subcooling, boiling, and pressure drop, and is well suited for system-level performance evaluation. The model is validated against a set of experimental data and demonstrates good agreement. The input parameters are varied over ranges representative of realistic data center operating conditions, and their influence on the effective footprint HTC is analyzed and discussed. This work provides practical insights into the parametric optimization of microchannel cold plate designs, supporting the development of efficient two-phase cooling solutions for next-generation high-performance data centers.

References

[1] D. Kulkarni, R. Tipton, E. Leka, J. Bankston, Q. Wang, and J. King. “Pumped 2P Refrigerant-Based Direct Liquid Cooling (DLC) Technology for Next Generation AI Clusters with High TDP Accelerators”, OCP White Paper, 2025.

[2] Q. Wang, S. Ozguc, and R. W. Bonner. “Systematic Analysis of Thermal Resistances in Data Center Two-Phase Direct-to-Chip Cooling.” International Electronic Pa ckaging Technical Conference and Exhibition. Vol. 89299. American Society of Mechanical Engineers, 2025.

[3] Q. Wang, S. Ozguc, A. Narayanan, and R. W. Bonner. “A Server-Level Test System for Direct-To-Chip Two-Phase Cooling of Data Centers Using a Low Global Warming Potential Fluid.” 2024 23rd IEEE Intersociety Conference on Thermal and Thermomechanical Phenomena in Electronic Systems (ITherm). IEEE, 2024.

[4] A. Narayanan, Q. Wang, S. Ozguc, and R. W. Bonner. “Investigation of Server Level Direct-to-Chip Two-Phase Cooling Solution for High Power GPUs.” International Electronic Packaging Technical Conference and Exhibition. Vol. 88469. American Society of Mechanical Engineers, 2024.

[5] Q. Wang, A. Narayanan, S. Ozguc, J. D. Moore, and R. W. Bonner. “Performance Comparison of R1233zd(E) and R515B for Two-Phase Direct-to-Chip Cooling.” 2025 24th IEEE Intersociety Conference on Thermal and Thermomechanical Phenomena in Electronic Systems (ITherm). IEEE, 2025.

[6] S. Ozguc, Q. Wang, A. Narayanan, J. Moore, and R. W. Bonner. “Design Optimization of Manifold Integrated Skived Cold Plates for Two-Phase Flow-Boiling.” 2025 41st Semiconductor Thermal Measurement, Modeling & Management Symposium (SEMI-THERM). IEEE, 2025.

[7] A. Narayanan, Q. Wang, S. Ozguc, T. Whitaker, J. Moore, and R. W. Bonner. “Direct on Die Two Phase Cooling Approach for High Power GPUs.” International Electronic Packaging Technical Conference and Exhibition. Vol. 89299. American Society of Mechanical Engineers, 2025.

[8] A. Patel, K. Yogi, G. Sahu, and T. Wei. “Direct-on-chip two-phase jet impingement cooling of multichip packages: Distributed inlet-outlet nozzles.” International Journal of Heat and Mass Transfer 252 (2025): 127514.

[9] S. Ozguc, Q. Wang, A. Narayanan, and R. W. Bonner. “Investigation of Flow Restrictors for Rack Level Two-Phase Cooling Under Nonuniform Heating.” 2024 40th Semiconductor Thermal Measurement, Modeling & Management Symposium (SEMI-THERM). IEEE, 2024.

[10] H. J. Cho, D. J. Preston, Y. Zhu, and E. N. Wang. “Nanoengineered materials for liquid–vapour phase-change heat transfer.” Nature Reviews Materials 2.2 (2016): 1-17.

[11] X. Liu, et al. “Enhancing Liquid–Vapor Phase-Change Heat Transfer with Micro/Nano-Structured Surfaces.” ACS Nano 19.10 (2025): 9513-9589.

[12] Q. Wang, and R. Chen. “Ultrahigh flux thin film boiling heat transfer through nanoporous membranes.” Nano Letters 18.5 (2018): 3096-3103.

[13] D. Kulkarni, J. Gulick, J. King, B. Jarrett, P. George, and Y. Feldman. “Thermal Performance of Common Cold Plate for Pumped Single- and Two-Phase Direct Liquid Cooling for Next Generation High Power Server Processors.” International Electronic Packaging Technical Conference and Exhibition. Vol. 88469. American Society of Mechanical Engineers, 2024.

[14] Q. Wang, D. P. Kulkarni, R. W. Bonner, and J. C. Gulick. “Universal Direct-to-Chip Cold Plates for Single- and Two-Phase Cooling.” 2024 OCP Global Summit Future Technologies Symposium, 2024.

[15] Q. Wang, and R. W. Bonner, “High-Performance Two-Phase Cooling under Different Cold Plate Orientations.” 2025 OCP EMEA Summit Future Technologies Symposium, 2025.

[16] H. Wang, Y. Qiu, J. Carter, J. McGuffin-Cawley, and C. R. Kharangate. “Effects of heating orientation on flow boiling in copper manifold microchannel heat sinks.” Experimental Thermal and Fluid Science 169 (2025): 111553.

[17] S. G. Kandlikar. “Fundamental issues related to flow boiling in minichannels and microchannels.” Experimental Thermal and Fluid Science 26.2-4 (2002): 389-407.

[18] J. R. Thome. “State-of-the-art overview of boiling and two-phase flows in microchannels.” Heat Transfer Engineering 27.9 (2006): 4-19.

[19] S. G. Kandlikar. “History, advances, and challenges in liquid flow and flow boiling heat transfer in microchannels: a critical review.” ASME Journal of Heat Transfer 134.3 (2012): 034001.

[20] G. Wang, L. Hao, and P. Cheng. “A four-zone model for saturated flow boiling in a microchannel of rectangular cross-section.” International Journal of Heat and Mass Transfer 53.17-18 (2010): 3439-3448.

[21] S. Jain, P. Jayaramu, and S. Gedupudi. “Modeling of pressure drop and heat transfer for flow boiling in a mini/micro-channel of rectangular cross-section.” International Journal of Heat and Mass Transfer 140 (2019): 1029-1054.

[22] Q. Wang, S. Ozguc, and R. W. Bonner. “A Practical Metric for Cold Plate Thermal Performance in Two-Phase Direct-to-Chip Cooling.” 2025 41st Semiconductor Thermal Measurement, Modeling & Management Symposium (SEMI-THERM). IEEE, 2025.

[23] K. P. Drummond, et al. “A hierarchical manifold microchannel heat sink array for high-heat-flux two-phase cooling of electronics.” International Journal of Heat and Mass Transfer 117 (2018): 319-330.

[24] E.W. Lemmon, I. H. Bell, M. L. Huber, and M. O. McLinden. NIST Standard Reference Database 23: Reference Fluid Thermodynamic and Transport Properties-REFPROP, Version 10.0, National Institute of Standards and Technology, Standard Reference Data Program, Gaithersburg, 2018.

[25] J. G. Collier, and J. R. Thome. Convective boiling and condensation. Clarendon Press, 1994.

[26] S. G. Kandlikar, S. Garimella, D. Li, S. Colin, and M. R. King. Heat transfer and fluid flow in minichannels and microchannels. Elsevier, 2006.

[27] S. M. Kim, and I. Mudawar. “Universal approach to predicting saturated flow boiling heat transfer in mini/micro-channels–Part II. Two-phase heat transfer coefficient.” International Journal of Heat and Mass Transfer 64 (2013): 1239-1256.

[28] S. M. Kim, and I. Mudawar. “Universal approach to predicting saturated flow boiling heat transfer in mini/micro-channels–Part I. Dryout incipience quality.” International Journal of Heat and Mass Transfer 64 (2013): 1226-1238.

[29] S. M. Kim, and I. Mudawar. “Thermal design and operational limits of two-phase micro-channel heat sinks.” International Journal of Heat and Mass Transfer 106 (2017): 861-876.

[30] W. Qu, and I. Mudawar. “Measurement and correlation of critical heat flux in two-phase micro-channel heat sinks.” International Journal of Heat and Mass Transfer 47.10-11 (2004): 2045-2059.

[31] S. M. Kim, and I. Mudawar. “Review of two-phase critical flow models and investigation of the relationship between choking, premature CHF, and CHF in micro-channel heat sinks.” International Journal of Heat and Mass Transfer 87 (2015): 497-511.

[32] G. B. Wallis. One-dimensional two-phase flow. McGraw-Hill, 1969.

[33] S. G. Kandlikar. “Heat transfer mechanisms during flow boiling in microchannels.” ASME Journal of Heat Transfer 126.1 (2004): 8-16.